Electronic Supplementary Information

Monitoring water harvesting in metal-organic frameworks, one water molecule at a time

Kelly M. Hunter*,† and Francesco Paesani*,†,‡,¶,§

†*Department of Chemistry and Biochemistry, University of California San Diego, La Jolla, California 92093, United States*

‡*Materials Science and Engineering, University of California San Diego, La Jolla, California 92093, United States*

¶*Halicioğlu Data Science Institute, University of California San Diego, La Jolla, California 92093, United States*

§*San Diego Supercomputer Center, University of California San Diego, La Jolla, California 92093, United States*

E-mail: k6hunter@ucsd.edu; fpaesani@ucsd.edu

MB-pol potential energy function for water

Since the MB-pol potential of water has already been described in detail in the literature,[1–3] we only overview here its salient features. MB-pol was derived from the many-body expansion (MBE) of the energy that allows for determining the energy, E_N, of an arbitrary system containing N (atomic or molecular) monomers as the sum of individual n-body energy contributions:

$$E_N(1,\ldots,N) = \sum_{i=1}^{N} \epsilon^{1\mathrm{B}}(i) + \sum_{i<j}^{N} \epsilon^{2\mathrm{B}}(i,j) + \sum_{i<j<k}^{N} \epsilon^{3\mathrm{B}}(i,j,k) + \cdots + \epsilon^{\mathrm{NB}}(1,\ldots,N) \tag{1}$$

Here, $\epsilon^{1\mathrm{B}}$ represents the distortion energy of an isolated monomer, such that $\epsilon^{1\mathrm{B}}(i) = E(i) - E_{\mathrm{eq}}(i)$ where $E_{\mathrm{eq}}(i)$ is the energy of the i-th monomer in its equilibrium geometry. The n-body energies, ϵ^{nB}, are defined recursively for $1 < n \leq N$ according to

$$\begin{aligned} \epsilon^{\mathrm{nB}} = E_{\mathrm{n}}(1,\ldots,n) - \sum_{i=1}^{N} \epsilon^{1\mathrm{B}}(i) - \sum_{i<j}^{N} \epsilon^{2\mathrm{B}}(i,j) - \sum_{i<j<k} \epsilon^{3\mathrm{B}}(i,j,k) - \cdots \\ \cdots - \sum_{i<j<k<\ldots}^{N} \epsilon^{(\mathrm{n}-1)\mathrm{B}}(i,j,k,\ldots,n-1) \end{aligned} \tag{2}$$

MB-pol approximates Eq. 2 as

$$E_N(1,..,N) = \sum_{i=1}^{N} \epsilon^{1\mathrm{B}}(i) + \sum_{i<j}^{N} \epsilon^{2\mathrm{B}}(i,j) + \sum_{i<j<k}^{N} \epsilon^{3\mathrm{B}}(i,j,k) + E_{\mathrm{POL}} \tag{3}$$

In MB-pol, the 1-body term ($\epsilon^{1\mathrm{B}}$) is represented by the potential developed by Partridge and Schwenke.[4] The 2-body term ($\epsilon^{2\mathrm{B}}$) describes four distinct contributions: permanent electrostatics, dispersion, 2-body polarization, and 2-body short-range interactions.[1] The 3-body term ($\epsilon^{3\mathrm{B}}$) describes two distinct contributions: 3-body polarization and 3-body short-range interactions.[2] The 2-body and 3-body short-range interactions are represented by 2-body and 3-body permutationally invariant polynomials (PIPs)[5] that were optimized in to reproduce 2-body and 3-body energies calculated at the CCSD(T) level of theory in the

complete basis set (CBS) limit.[1,2] In the actual implementation of MB-pol,[1,2] the 2-body and 3-body polarization contributions are implicitly included in the E_{POL} term of Eq. 3 which represents many-body interactions at all orders through a classical polarization term. Further details of the MB-pol potential can be found in the original references.[1–3]

By correctly representing both short- and long-range many-body interactions at all orders,[6] MB-pol has been shown to accurately predict structural, thermodynamic, dynamical, and spectroscopic properties of water, from gas-phase clusters to liquid water and ice.[7] To date, MB-pol is the only model that correctly predicts the phase diagram of water (Figure S1).[8]

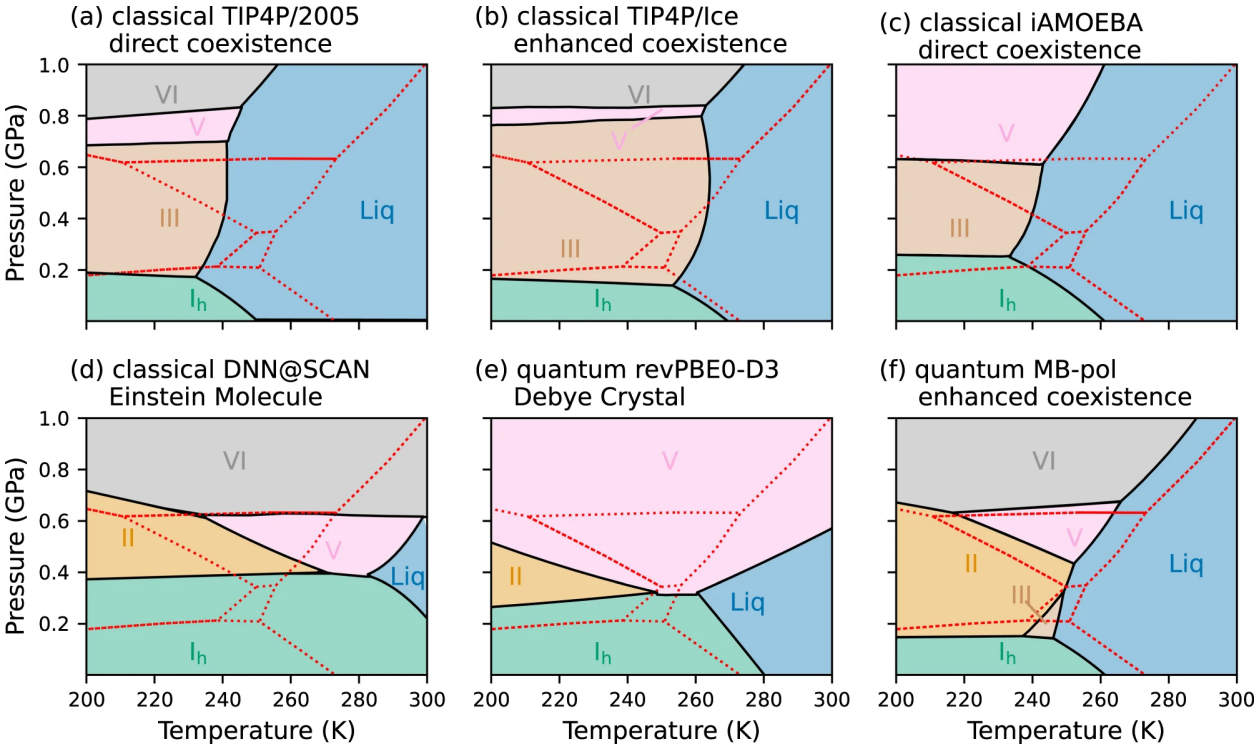

Figure S1: Phase diagram of water calculated with TIP4P/2005 (a), TIP4P/Ice (b), iAMOEBA (c), DNN@SCAN (d), revPBE0-D3 (e), MB-pol (f). The experimental phase diagram[9] is shown in each panel using a dotted red line. The region of stability for each ice polymorph I_h, II, III, V, VI and liquid phase are indicated colored area in green, orange, gray, brown, pink, and blue, respectively. See Ref. 8 for details. Figure adapted from S.L. Bore and F. Paesani, *Nat. Commun.* 14, 3349 (2023); licensed under a Creative Commons Attribution (CC BY) license.

The accuracy of MB-pol has been systematically assessed across the three phases of water through extensive comparisons with experimental data and high-level ab initio calculations in Ref. 7. More recently, an updated version of MB-pol, MB-pol(2023), trained on larger training sets of CCSD(T) many-body energies, has been shown to achieve even higher predictive accuracy for simulations of water in both gas and liquid phases.[10] In the following, we only highlights some of the MB-pol results that have been reported in the scientific literature since 2013 when MB-pol was first introduced.

Regarding the properties of gas-phase clusters, MB-pol quantitatively reproduces the vibration–rotation tunneling spectrum of the water dimer (Table S1),[1] the energetics, quantum isomeric equilibria, tunneling splittings, and vibrational spectra of small water clusters.[11–22]

Table S1: Experimental[23–27] and calculated VRT levels and tunneling splittings of $(H_2O)_2$: ground state (GS), donor torsion (DT), acceptor wag (AW), acceptor twist (AT), donor torsion overtone (DT2), and intermolecular stretch (OO). The energies (in cm^{-1}) correspond to the origins $o_1(K)$ and $o_2(K)$ of the levels (1) and (2) with quantum numbers $K = 0$ and $K = 1$, respectively. The values in parentheses are the interchange tunneling splittings $i_1(K)$ and $i_2(K)$. See Ref. 1 for details.

		Experiment	MB-pol		Experiment	MB-pol
OO	(2)	153.62(1.88)	154.79(2.20)	(1)		156.97(-2.45)
	(1)		149.08(1.84)	(2)		152.93(4.06)
DT[2]	(2)		185.20(17.9)	(2)		
	(1)		128.57(11.0)	(1)		
AT	(1)		129.52(-0.33)	(1)		143.79(4.76)
	(2)		119.32(10.00)	(2)		137.10(5.88)
AW	(2)		109.26(0.16)	(2)		124.02(3.62)
	(1)		108.83(2.99)	(1)		110.09(5.77)
DT	(1)		113.33(5.44)	(2)		91.10(3.37)
	(2)		61.26(2.50)	(1)		85.35(1.00)
GS	(2)		11.89(0.68)	(1)		14.92(0.75)
	(1)		0.00(0.80)	(2)		12.07(0.49)
		K=0			K=1	

Importantly, to date, MB-pol stands out as the only model that accurately reproduces the quantum ground states of the $(H_2O)_6$ and $(D_2O)_6$ clusters,[28] identifying the cage isomer as the ground state for the former and the prism isomer for the latter as well as the corresponding infrared spectra (Figure S2.[15] This distinction is noteworthy, especially since empirical water models fail to predict the correct energetics of these clusters.[29]

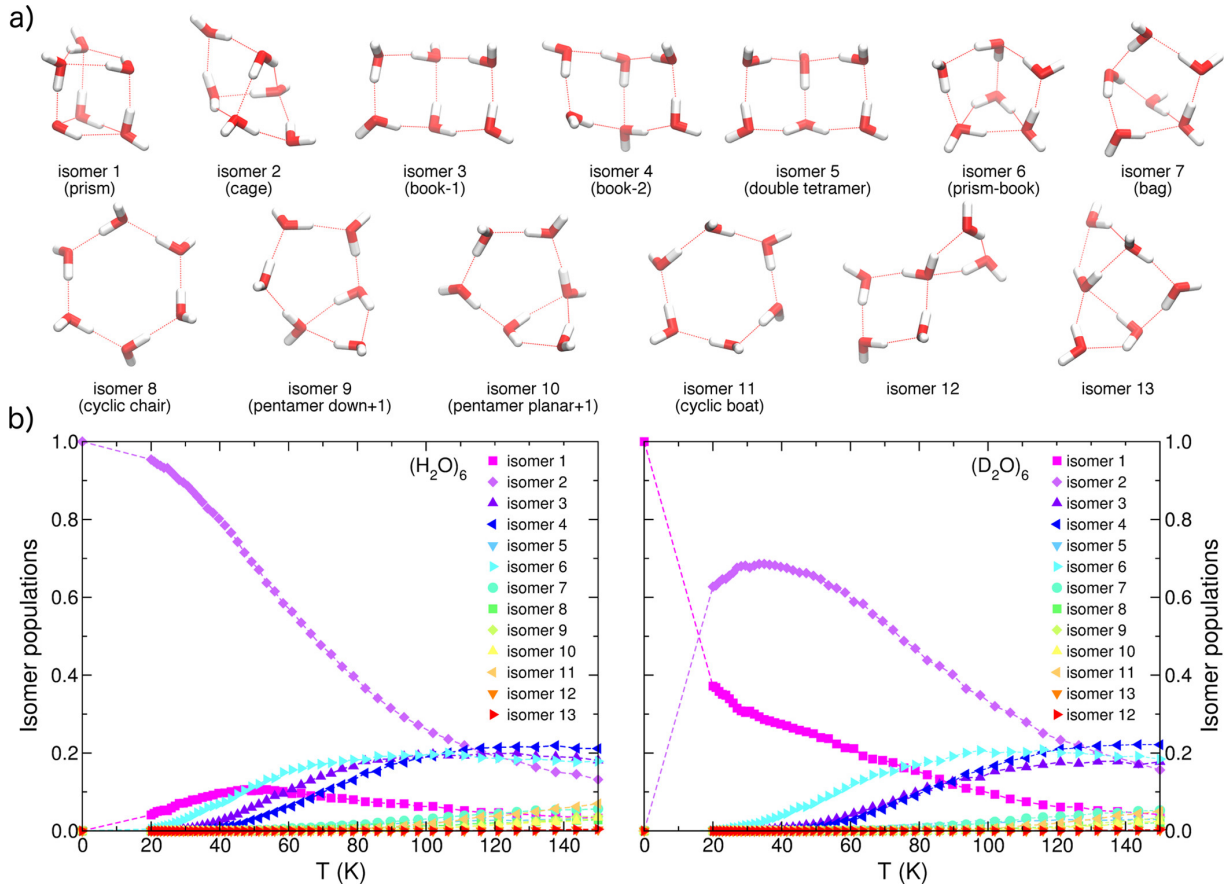

Figure S2: (a) Structures of the 13 low-lying isomers of the water hexamer determined from the positions of the O atoms. (b) Isomer populations of $(H_2O)_6$ (left) and $(D_2O)_6$ (right) obtained from replica exchange path-integral molecular dynamics (RE-PIMD) simulations with MB-pol. See Ref. 15 for details. Figure reprinted with permission from *J. Am. Chem. Soc.* 139, 7082-7088 (2017). Copyright 2017 American Chemical Society.

Regarding the properties of liquid water, MB-pol accurately reproduces structural, thermodynamic, and dynamical properties (e.g., see Figures S3, S4, S5)[7,30] as well as infrared, Raman, and X-ray spectra of liquid water (e.g., see Figure S6;[31–37] sum-frequency generation spectra of the air/water interface;[38–41] and vapor–liquid equilibrium properties (e.g., see

Figure S7,[42] from the critical point at the end of the vapor-liquid coexistence line down to supercooled temperatures.

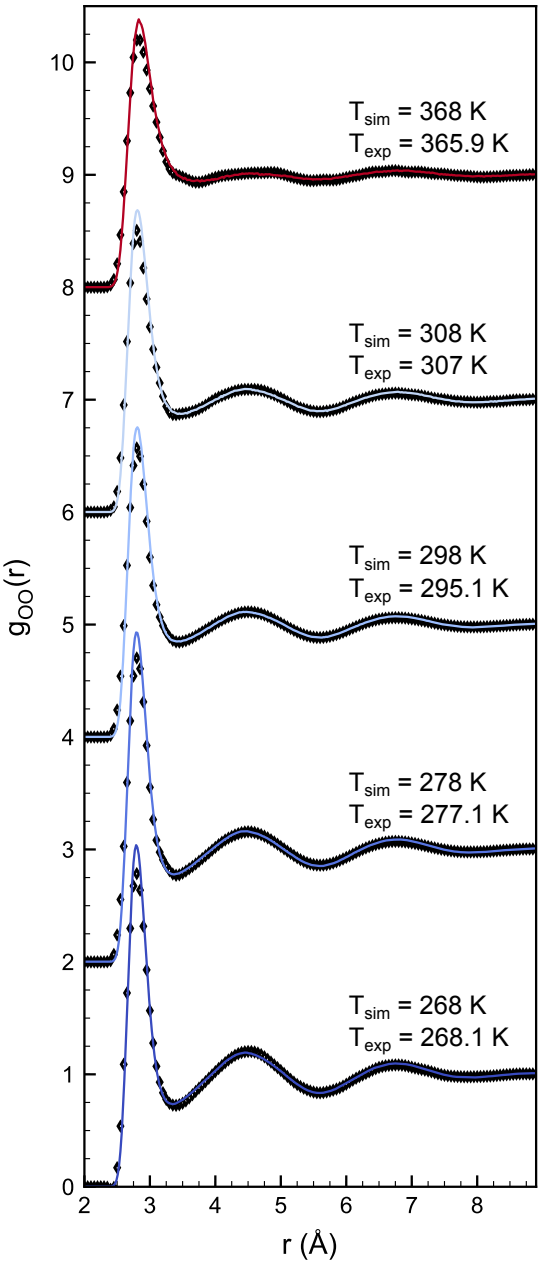

Figure S3: Structure of liquid water. Oxygen-oxygen radial distribution function, g_{OO}, for select simulation and experimental temperatures (T_{sim} and T_{exp}, respectively) as marked. Black symbols are experimental data from Ref. 43 and colorful lines are MB-pol results with N = 256. Different temperatures are shifted vertically for clarity. See Ref. 30 for details. Figure reprinted with permission from *J. Phys. Chem. Lett.* 13, 3652-3658 (2022). Copyright 2022 American Chemical Society.

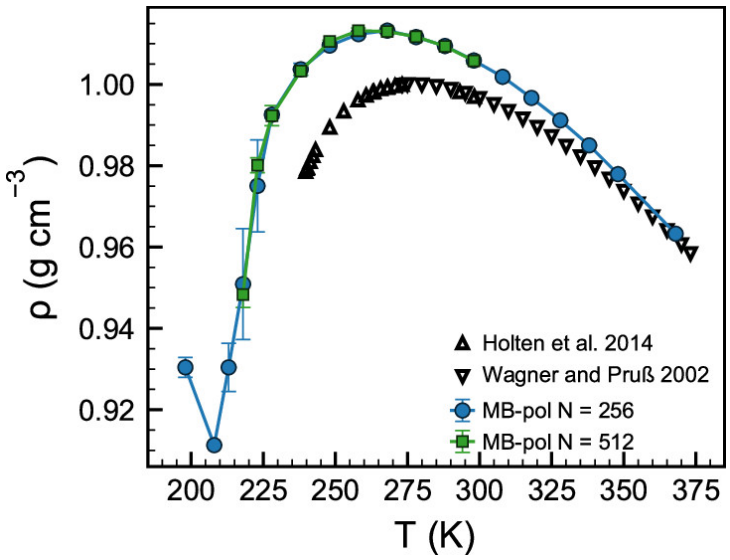

Figure S4: Mass density, ρ, of liquid water from experiments in Refs. 44 and 45 (black symbols) and as predicted by MB-pol with N = 256 (blue circles) and N = 512 (green squares). Error bars in simulation results represent 95% confidence intervals. See Ref. 30 for details. Figure reprinted with permission from *J. Phys. Chem. Lett.* 13, 3652-3658 (2022). Copyright 2022 American Chemical Society.

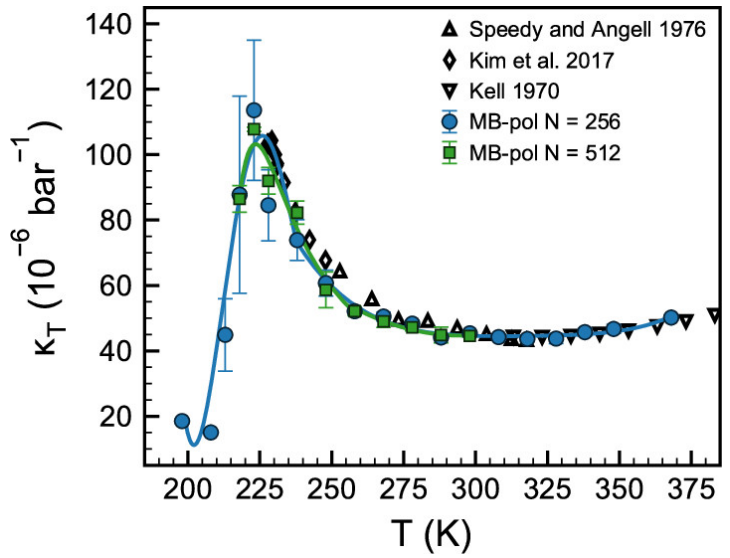

Figure S5: Isothermal compressibility, κ_T, from experiments in Refs. 46–48 (black symbols) and as predicted by MB-pol with N = 256 molecules (blue circles) and N = 512 molecules (green squares). See Ref. 30 for details. Figure reprinted with permission from *J. Phys. Chem. Lett.* 13, 3652-3658 (2022). Copyright 2022 American Chemical Society.

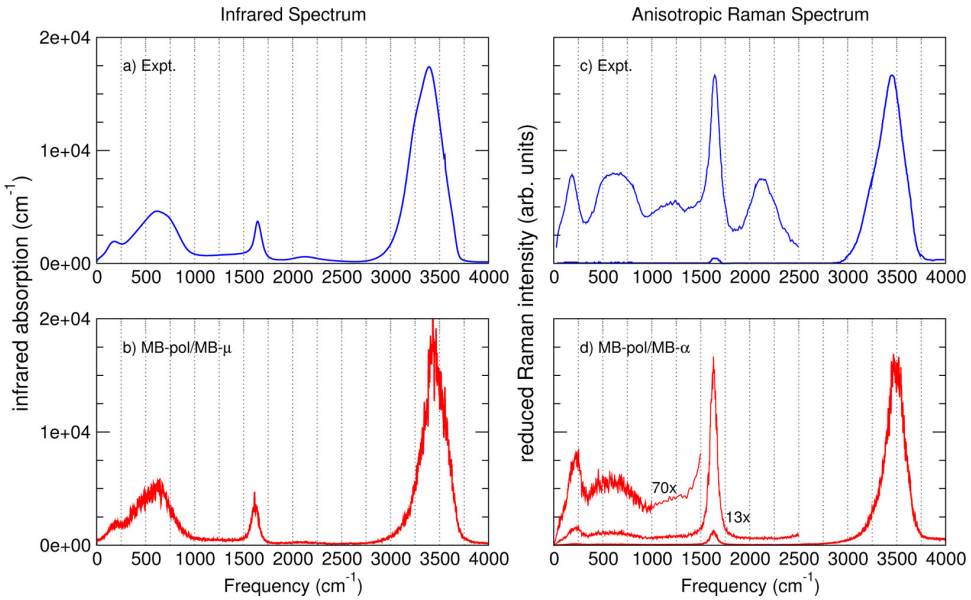

Figure S6: Experimental and MB-pol infrared (a, b) and reduced anisotropic Raman spectra (c, d) of liquid water under ambient conditions. See Ref. 31 for details. Figure reprinted with permission from *J. Chem. Theory Comput.* 11, 1145-1154 (2015). Copyright 2015 American Chemical Society.

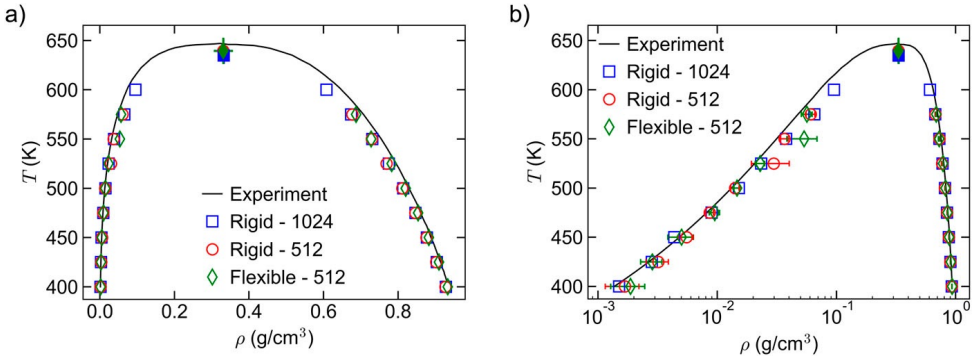

Figure S7: (a) Vapor–liquid coexistence curves (vapor and liquid mass densities ρ as a function of temperature T) for the three different cases studied: MB-pol rigid model with 512 molecules (red circles), MB-pol rigid model with 1024 molecules (blue squares), and MB-pol flexible model with 512 molecules (green diamonds). (b) Same data as (a) presented on a log-scale in ρ to display the vapor phase densities. In both panels, coexistence densities are represented as open symbols, estimated critical points are represented as filled symbols, and experimental data52 are shown as solid lines. Statistical uncertainties are at the 95% confidence level and are shown only when larger than the symbol size. See Ref. 42 for details. Figure reprinted from J. Chem. Phys. 154, 211103 (2021), with the permission of AIP Publishing.

The ability of MB-pol to accurately predict structural, thermodynamic, and dynamical properties of liquid water across a wide temperature range is particularly pertinent to the modeling of water adsorption in MOFs as the behavior of water in confinement mirrors that of supercooled water. Equally important is the ability of MB-pol to accurately capture vapor–liquid equilibrium coexistence properties, as these are crucial in determining the pore-filling stage of the adsorption process.

Regarding the properties of ice, MB-pol has demonstrated its capability to accurately reproduce the lattice energies of various ice polymorphs,[49] as well as the infrared and Raman spectra of ice I_h[50] and all ordered phases of ice.[51] The remarkable accuracy of MB-pol in reproducing vibrational spectra of water across gas-phase clusters, liquid water, and ice is particularly noteworthy. This accuracy is crucial for characterizing the adsorption mechanisms of water in MOFs, as it enables a detailed connection between macroscopic thermodynamics and molecular-level insights into binding and hydrogen-bonding motifs.

Force field development and force field parameters

Fig. S8 shows the atom labels used in the definition of the flexible force field parameters for Ni_2X_2BTDD.

The General Amber Force Field (GAFF)[52] was used to model the intramolecular interactions of the organic linker, while the force field parameters associated with the description of all bonds, angles, and dihedrals involving the Ni^{2+} metal centers were obtained from potential energy scans of the Ni atom along the reduced molecular model in Fig. S8A. These calculations were carried out with Gaussian 16[53] at the DFT level using the ωB97X-D functional[54] in combination with the def2-TZVP basis set.[55] The actual fits were performed using a genetic algorithm on 253, 252, and 252 distorted configurations for Ni_2F_2BTDD, Ni_2Cl_2BTDD, and Ni_2Br_2BTDD, respectively, obtained by displacing the Ni atom along the

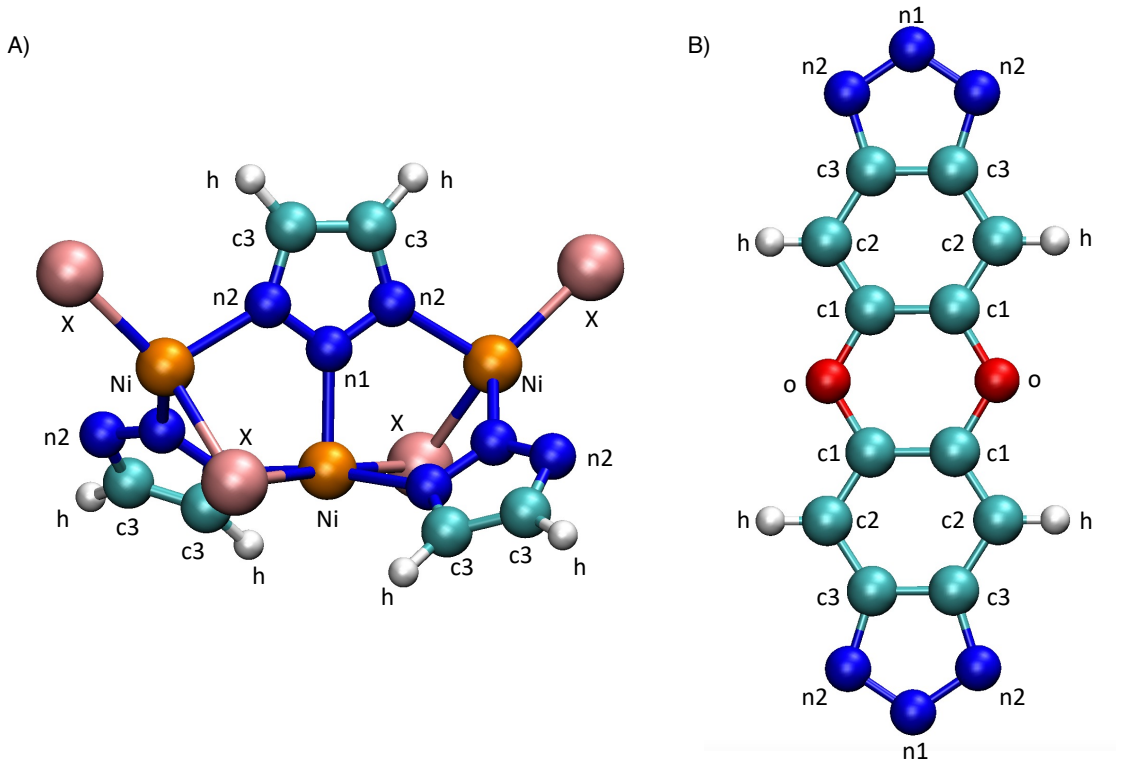

Figure S8: **Atom names for the Ni_2X_2BTDD MOFs.** Atom names for the A) metal cluster and B) organic linker of the Ni_2X_2BTDD MOFs. The atom label "X" corresponds to the F, Cl, or Br halide atom in each MOF.

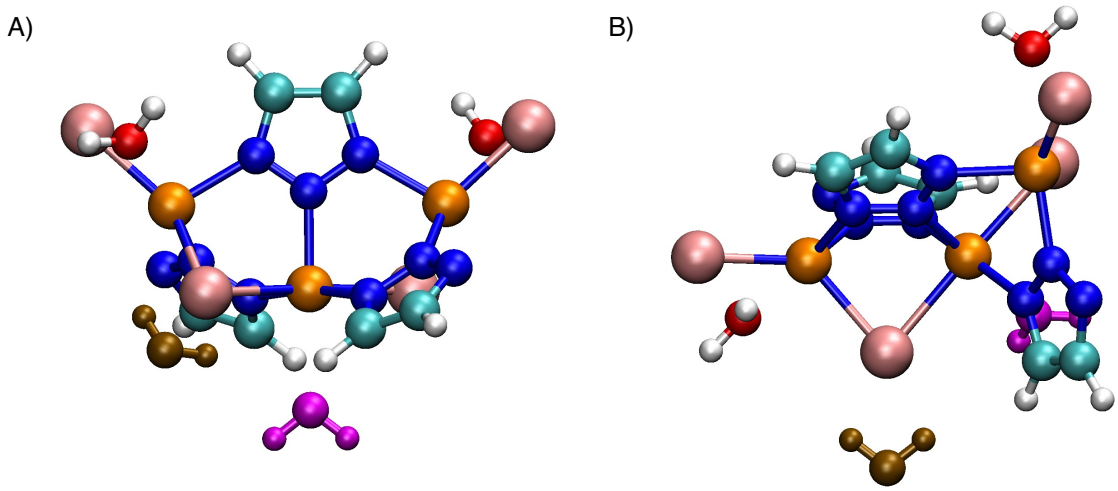

Figure S9: **Water scans for the Ni_2X_2BTDD MOFs.** A) Scan of the magenta water molecule away from the Ni^{2+} metal center to fit the Ni–OW nonbonded parameter. All other water molecules were kept fixed. B) Scan of the brown water molecule away from the halide atom to fit the OW–X and HW–X nonbonded parameters. All other water molecules were kept fixed. The atom "X" corresponds to the F, Cl, or Br halide atoms in each MOF, while OW and HW indicate the oxygen and hydrogen atoms of a water molecule.

x, y, and z directions. This process was repeated for each MOF (Ni_2F_2BTDD, Ni_2Cl_2BTDD, and Ni_2Br_2BTDD) to ensure an accurate description of the interaction of the Ni^{2+} metal center with the halide atom.

The MOF–water interactions were obtained from a combination of potential energy scans of a water molecule away from the Ni^{2+} metal center (Fig. S9A) and away from the halide atom (Fig. S9B). These calculations were analogously carried out with Gaussian 16[53] at the DFT level using the ωB97X-D functional[54] in combination with the def2-TZVP basis set.[55] The actual fits were performed using a genetic algorithm on 100, 88, and 76 distorted configurations for Ni_2F_2BTDD, Ni_2Cl_2BTDD, and Ni_2Br_2BTDD, respectively, obtained by displacing the water molecule in a one-dimensional scan away from the Ni^{2+} metal center or the halide atom. This process was repeated for each MOF (Ni_2F_2BTDD, Ni_2Cl_2BTDD, and Ni_2Br_2BTDD) to ensure an accurate description of the water molecule with the open Ni^{2+} metal center and with the halide atom.

The complete list of parameters for the Ni_2F_2BTDD, Ni_2Cl_2BTDD, and Ni_2Br_2BTDD force fields is reported in Tables S2-S16.

Table S2: Force field parameters for the Ni_2F_2BTDD force field. Electrostatic and Lennard-Jones potentials.

Atom name	Atom type	Charge	ϵ (kcal $\cdot$ mol^{-1})	$\sigma/2$ (Å)
Ni	Ni	0.996843	0.015000	1.262400
f	f	-0.425177	0.050000	1.498500
n1	n	-0.136514	0.170100	1.625000
n2	n	-0.271968	0.170100	1.625000
c1	c	0.074039	0.086050	1.700000
c2	c	-0.107718	0.086050	1.700000
c3	c	0.072102	0.086050	1.700000
h	h	0.108596	0.015010	1.300000
o	o	-0.185254	0.210000	1.480000

Table S3: Force field parameters for the Ni_2F_2BTDD force field. Water–MOF Buckingham potentials.

Buckingham pair	A	ρ	C
OW-Ni	34373.41	0.253835	62.1224
OW-f	72009.25	0.250107	999.944
HW-f	99999.14	0.179166	121.088

Table S4: Force field parameters for the Ni_2F_2BTDD force field. Bond potentials: Harmonic functions.

Bond type (Harmonic)	K_{ij} (kcal $\cdot$ mol^{-1} $\cdot$ Å^2)	r_0 (Å)
Ni-f	126.80	2.38
Ni-n	275.20	2.02
n-n	1714.80	1.22
n-c	935.40	1.35
c-c	922.20	1.40
c-h	691.60	1.086
c-o	735.20	1.37

Table S5: Force field parameters for the Ni_2F_2BTDD force field. Bending potentials.

Angle type (Harmonic)	K_{ijk} (kcal $\cdot$ mol^{-1} $\cdot$ rad^2)	θ (°)
Ni-f-Ni	17.80	101.80
f-Ni-f	11.70	178.00
f-Ni-n	14.90	122.00
Ni-n-n	146.20	126.40
Ni-n-c	41.60	115.50
n-Ni-n	13.30	126.30
n-n-n	52.10	110.75
n-n-c	151.10	112.10
n-c-c	138.90	119.72
c-c-c	133.20	120.02
c-c-h	96.36	119.88
c-c-o	139.16	119.20
c-o-c	126.96	119.89

Table S6: Force field parameters for the Ni_2F_2BTDD force field. Torsion potentials.

Dihedral type	K_{ijkl} (kcal · mol^{-1})	χ (°)	N
Ni-f-Ni-f	0.0000	180.00	2
Ni-f-Ni-n	3.0149	0.00	2
f-Ni-n-n	1.7925	180.00	2
f-Ni-n-c	2.2350	180.00	2
Ni-n-n-Ni	0.3567	0.00	2
Ni-n-n-c	0.5781	180.00	2
Ni-n-c-c	4.8540	180.00	2
Ni-n-n-n	3.5080	180.00	2
n-Ni-n-c	0.0000	0.00	2
n-Ni-n-n	0.0000	0.00	2
n-n-c-c	4.8000	180.00	2
n-n-n-c	0.0000	180.00	2
n-c-c-n	3.6250	180.00	2
n-c-c-c	3.6250	180.00	2
n-c-c-h	3.6250	180.00	2
c-c-c-h	3.6250	180.00	2
c-c-c-c	3.6250	180.00	2
c-c-c-o	3.6250	180.00	2
c-c-o-c	0.9000	180.00	2
o-c-c-o	3.6250	180.00	2
o-c-c-h	3.6250	180.00	2
c-n-c-c	1.1000	180.00	2
c-c-c-h	1.1000	180.00	2
c-c-c-o	1.1000	180.00	2

Table S7: Force field parameters for the Ni_2Cl_2BTDD force field. Electrostatic and Lennard-Jones potentials.

Atom name	Atom type	Charge	ϵ (kcal · mol^{-1})	$\sigma/2$ (Å)
Ni	Ni	0.926482	0.015000	1.262400
cl	cl	-0.348231	0.227000	1.758200
n1	n	-0.136863	0.170100	1.625000
n2	n	-0.275086	0.170100	1.625000
c1	c	0.074039	0.086050	1.700000
c2	c	-0.107718	0.086050	1.700000
c3	c	0.072102	0.086050	1.700000
h	h	0.108596	0.015010	1.300000
o	o	-0.185254	0.210000	1.480000

Table S8: Force field parameters for the Ni_2Cl_2BTDD force field. Water–MOF Buckingham potentials.

Buckingham pair	A	ρ	C
OW-Ni	61959.99	0.226578	119.128
OW-cl	23436.28	0.313515	499.725
HW-cl	28034.52	0.259469	300.924

Table S9: Force field parameters for the Ni_2Cl_2BTDD force field. Bond potentials: Harmonic functions.

Bond type (Harmonic)	K_{ij} (kcal $\cdot$ mol^{-1} $\cdot$ Å^2)	r_0 (Å)
Ni-cl	72.90	2.25
Ni-n	183.70	2.02
n-n	1714.80	1.22
n-c	935.40	1.35
c-c	922.20	1.40
c-h	691.60	1.086
c-o	735.20	1.37

Table S10: Force field parameters for the Ni_2Cl_2BTDD force field. Bending potentials.

Angle type (Harmonic)	K_{ijk} (kcal $\cdot$ mol^{-1} $\cdot$ rad^2)	θ (°)
Ni-cl-Ni	62.40	77.30
cl-Ni-cl	63.60	179.40
cl-Ni-n	12.10	86.80
Ni-n-n	112.90	131.60
Ni-n-c	29.80	106.90
n-Ni-n	10.90	127.00
n-n-n	52.10	110.75
n-n-c	151.10	112.10
n-c-c	138.90	119.72
c-c-c	133.20	120.02
c-c-h	96.36	119.88
c-c-o	139.16	119.20
c-o-c	126.96	119.89

Table S11: Force field parameters for the Ni_2Cl_2BTDD force field. Torsion potentials.

Dihedral type	K_{ijkl} (kcal · mol^{-1})	χ (°)	N
Ni-cl-Ni-cl	0.0000	180.00	2
Ni-cl-Ni-n	2.9292	0.00	2
cl-Ni-n-n	1.8350	180.00	2
cl-Ni-n-c	3.6679	180.00	2
Ni-n-n-Ni	4.5489	0.00	2
Ni-n-n-c	0.4848	180.00	2
Ni-n-c-c	4.6947	180.00	2
Ni-n-n-n	3.4319	180.00	2
n-Ni-n-c	0.0000	0.00	2
n-Ni-n-n	0.0000	0.00	2
n-n-c-c	4.8000	180.00	2
n-n-n-c	0.0000	180.00	2
n-c-c-n	3.6250	180.00	2
n-c-c-c	3.6250	180.00	2
n-c-c-h	3.6250	180.00	2
c-c-c-h	3.6250	180.00	2
c-c-c-c	3.6250	180.00	2
c-c-c-o	3.6250	180.00	2
c-c-o-c	0.9000	180.00	2
o-c-c-o	3.6250	180.00	2
o-c-c-h	3.6250	180.00	2
c-n-c-c	1.1000	180.00	2
c-c-c-h	1.1000	180.00	2
c-c-c-o	1.1000	180.00	2

Table S12: Force field parameters for the Ni_2Br_2BTDD force field. Electrostatic and Lennard-Jones potentials.

Atom name	Atom type	Charge	ϵ (kcal · mol^{-1})	$\sigma/2$ (Å)
Ni	Ni	0.891763	0.015000	1.262400
br	br	-0.307722	0.251000	1.866000
n1	n	-0.137971	0.170100	1.625000
n2	n	-0.277427	0.170100	1.625000
c1	c	0.074039	0.086050	1.700000
c2	c	-0.107718	0.086050	1.700000
c3	c	0.072102	0.086050	1.700000
h	h	0.108596	0.015010	1.300000
o	o	-0.185254	0.210000	1.480000

Table S13: Force field parameters for the Ni_2Br_2BTDD force field. Water–MOF Buckingham potentials.

Buckingham pair	A	ρ	C
OW-Ni	149772.98	0.203026	244.993
OW-br	99756.15	0.317524	1991.79
HW-br	199964.33	0.179652	249.365

Table S14: Force field parameters for the Ni_2Br_2BTDD force field. Bond potentials: Harmonic functions.

Bond type (Harmonic)	K_{ij} (kcal $\cdot$ mol^{-1} $\cdot$ Å^2)	r_0 (Å)
Ni-br	50.80	2.46
Ni-n	209.20	1.99
n-n	1714.80	1.22
n-c	935.40	1.35
c-c	922.20	1.40
c-h	691.60	1.086
c-o	735.20	1.37

Table S15: Force field parameters for the Ni_2Br_2BTDD force field. Bending potentials.

Angle type (Harmonic)	K_{ijk} (kcal $\cdot$ mol^{-1} $\cdot$ rad^2)	θ (°)
Ni-br-Ni	19.50	75.10
br-Ni-br	13.60	170.50
br-Ni-n	16.90	108.60
Ni-n-n	128.30	120.60
Ni-n-c	56.30	102.50
n-Ni-n	11.90	128.60
n-n-n	52.10	110.80
n-n-c	151.10	112.10
n-c-c	138.90	119.72
c-c-c	133.20	120.02
c-c-h	96.36	119.88
c-c-o	139.16	119.20
c-o-c	126.96	119.89

Table S16: Force field parameters for the Ni_2Br_2BTDD force field. Torsion potentials.

Dihedral type	K_{ijkl} (kcal $\cdot$ mol^{-1})	χ (°)	N
Ni-br-Ni-br	0.0000	180.00	2
Ni-br-Ni-n	2.5866	0.00	2
br-Ni-n-n	4.6775	180.00	2
br-Ni-n-c	0.6373	180.00	2
Ni-n-n-Ni	4.6914	0.00	2
Ni-n-n-c	0.7777	180.00	2
Ni-n-c-c	4.4819	180.00	2
Ni-n-n-n	3.3928	180.00	2
n-Ni-n-c	0.0000	0.00	2
n-Ni-n-n	0.0000	0.00	2
n-n-c-c	4.8000	180.00	2
n-n-n-c	0.0000	180.00	2
n-c-c-n	3.6250	180.00	2
n-c-c-c	3.6250	180.00	2
n-c-c-h	3.6250	180.00	2
c-c-c-h	3.6250	180.00	2
c-c-c-c	3.6250	180.00	2
c-c-c-o	3.6250	180.00	2
c-c-o-c	0.9000	180.00	2
o-c-c-o	3.6250	180.00	2
o-c-c-h	3.6250	180.00	2
c-n-c-c	1.1000	180.00	2
c-c-c-h	1.1000	180.00	2
c-c-c-o	1.1000	180.00	2

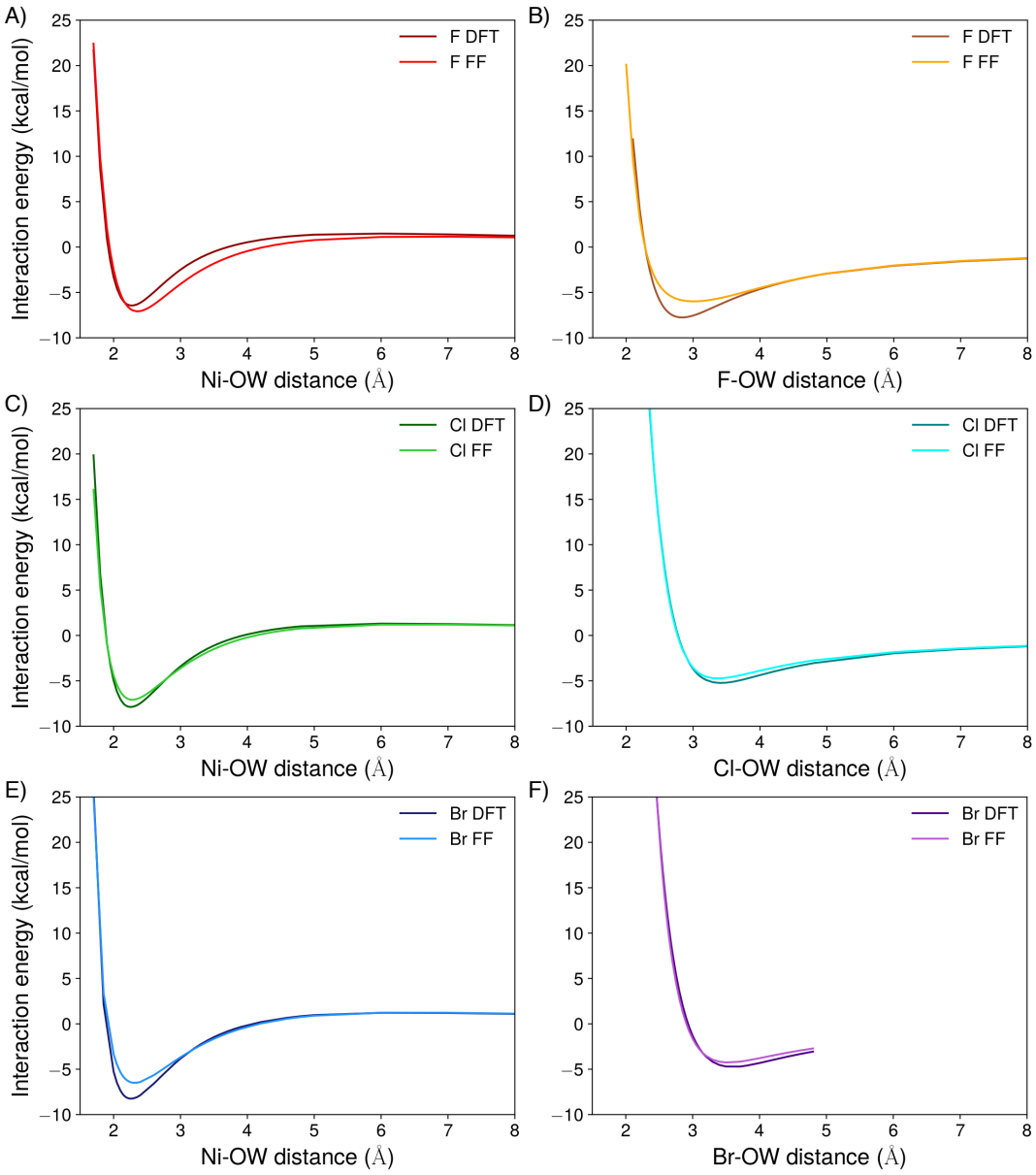

Figure S10: **Evaluation of the Ni_2X_2BTDD force fields against DFT.** Scans of water away from the Ni^{2+} metal center in A) Ni_2F_2BTDD, C) Ni_2Cl_2BTDD, and E) Ni_2Br_2BTDD. Scans away from the Ni^{2+} metal center are the same as in Fig. S9A. Scans of water away from the B) fluoride atom in Ni_2F_2BTDD, D) chloride atom in Ni_2Cl_2BTDD, and F) bromide atom in Ni_2Br_2BTDD. Scans away from the halide atom as the same as in Fig. S9B. DFT calculations shown in darker colors, and force field calculations shown in lighter colors.

Structure, thermodynamics, and spectroscopy

The theoretical IR spectra at all water loadings were calculated within the time-dependent formalism according to

$$I_{IR} = \left[\frac{2\omega}{3V\hbar c\epsilon_0}\right] tanh\left(\beta\hbar\omega\right) \int_{-\infty}^{\infty} e^{i\omega t} \left\langle \mu(0)\mu(t)\right\rangle dt \tag{4}$$

where V is the system volume, c is the speed of light in vacuum, ϵ_0 is the permittivity of free space, and $\beta = (k_B T)^{-1}$, with k_B being Boltzmann's constant. In Eq. 4, $\langle \mu(0)\mu(t)\rangle$ is the ensemble-averaged dipole-dipole time correlation function that was calculated by averaging over all the NVE trajectories at each water loading, with μ being represented by the MB-μ many-body dipole moment function.[31]

The density of states (DOS) spectra were calculated within the time-dependent formalism using

$$I_{DOS} = \int_{-\infty}^{\infty} e^{i\omega t} \left\langle v(0)v(t)\right\rangle dt \tag{5}$$

where $\langle v(0)v(t)\rangle$ is the ensemble-averaged classical velocity-velocity autocorrelation function.

The enthalpy of adsorption at each water loading was calculated using

$$\Delta H = \frac{E_{MOF+wat} - E_{MOF} - [(N_{wat} \times E_{wat}) + (N_{wat} \times R \times T)]}{N_{wat}} \tag{6}$$

where $E_{MOF+wat}$ is the energy of the MOF + water system, E_{MOF} is the energy of the empty MOF, E_{wat} is the energy of a single MB-pol water molecule, N_{wat} is the number of water molecules at each loading, R is the gas constant, and T is the system temperature. The entropy at each water loading was calculated according to the two-phase thermodynamic (2PT) model.[56–58]

The H-bond correlation function was calculated using

$$c(t) = \frac{\langle h(0)\, h(t)\rangle}{\langle h\rangle} \tag{7}$$

where $\langle h(0)\, h(t)\rangle$ is the ensemble-averaged H-bond correlation function.[59] The function $h(t)$ has a value of 0 if water does not form a H-bond to one of the MOF atoms at time t, and $h(t)$ has a value of 1 if water forms a H-bond to one of the MOF atoms at time t. $\langle h\rangle$ is the average of the H-bond correlation function.

Table S17: Simulation cell dimensions for the Ni_2F_2BTDD force field. All cell dimensions calculated from a 1 ns NPT simulation at 300 K except for the empty MOF, which were calculated from a 1 ns NPT simulation at 100 K to compare to the experimental cell dimensions.

Water loading	x/y (Å)	z (Å)
Experiment (100 K)	38.6092	8.09293
Empty MOF (100 K)	38.0765	8.09063
54 (1 H_2O/Ni)	38.0630	8.08780
108 (2 H_2O/Ni)	38.0347	8.08177
162 (3 H_2O/Ni)	38.0071	8.07590
216 (4 H_2O/Ni)	37.9826	8.07070
270 (5 H_2O/Ni)	37.9678	8.06757
324 (6 H_2O/Ni)	37.9529	8.06440
378 (7 H_2O/Ni)	37.9384	8.06130
432 (8 H_2O/Ni)	37.9163	8.05663
486 (9 H_2O/Ni)	37.8934	8.05173
540 (10 H_2O/Ni)	37.8683	8.04640
594 (11 H_2O/Ni)	37.8273	8.03770
648 (12 H_2O/Ni)	37.8045	8.03287

Table S18: Simulation cell dimensions for the Ni_2Cl_2BTDD force field. All cell dimensions calculated from a 1 ns NPT simulation at 300 K except for the empty MOF, which were calculated from a 1 ns NPT simulation at 100 K to compare to the experimental cell dimensions.

Water loading	x/y (Å)	z (Å)
Experiment (100 K)	38.5282	8.18879
Empty MOF (100 K)	38.4682	7.92367
54 (1 H_2O/Ni)	38.4332	7.91647
108 (2 H_2O/Ni)	38.3873	7.90700
162 (3 H_2O/Ni)	38.3390	7.89707
216 (4 H_2O/Ni)	38.3174	7.89260
270 (5 H_2O/Ni)	38.2972	7.88847
324 (6 H_2O/Ni)	38.2719	7.88323
378 (7 H_2O/Ni)	38.2598	7.88073
432 (8 H_2O/Ni)	38.2216	7.87287
486 (9 H_2O/Ni)	38.1944	7.86727
540 (10 H_2O/Ni)	38.1550	7.85917
594 (11 H_2O/Ni)	38.1130	7.85050
648 (12 H_2O/Ni)	38.1412	7.85630
702 (13 H_2O/Ni)	38.2220	7.87297

Table S19: Simulation cell dimensions for the Ni_2Br_2BTDD force field. All cell dimensions calculated from a 1 ns NPT simulation at 300 K except for the empty MOF, which were calculated from a 1 ns NPT simulation at 100 K to compare to the experimental cell dimensions.

Water loading	x/y (Å)	z (Å)
Experiment (100 K)	38.4250	8.20774
Empty MOF (100 K)	38.4062	7.96167
54 (1 H_2O/Ni)	38.2658	7.93253
108 (2 H_2O/Ni)	38.0679	7.89153
162 (3 H_2O/Ni)	37.9888	7.87513
216 (4 H_2O/Ni)	37.9616	7.86950
270 (5 H_2O/Ni)	37.8911	7.85487
324 (6 H_2O/Ni)	37.8521	7.94680
378 (7 H_2O/Ni)	37.7982	7.83560
432 (8 H_2O/Ni)	37.7337	7.82223
486 (9 H_2O/Ni)	37.6669	7.80840
540 (10 H_2O/Ni)	37.5792	7.79020
594 (11 H_2O/Ni)	37.5753	7.78940

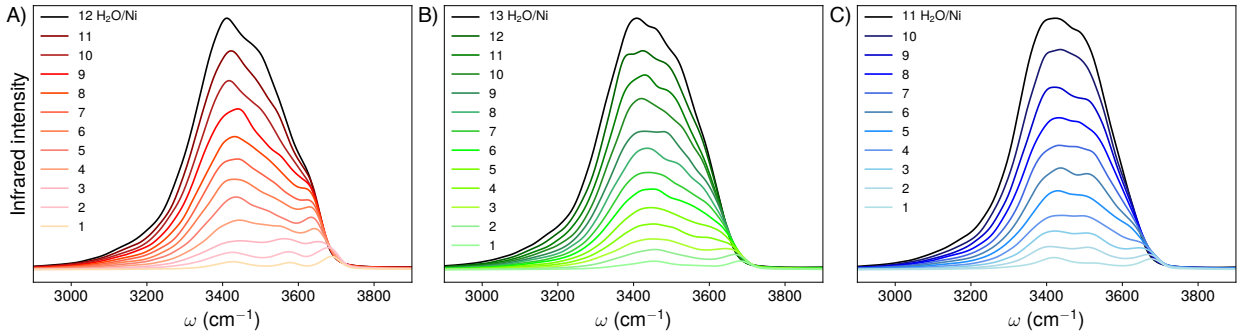

Figure S11: **Infrared spectra of water in Ni_2X_2BTDD at all loadings.** A) IR spectra of water confined in Ni_2F_2BTDD from 12 H_2O/Ni^{2+} (dark red) to 1 H_2O/Ni^{2+} (light red). B) IR spectra of water confined in Ni_2Cl_2BTDD from 13 H_2O/Ni^{2+} (dark green) to 1 H_2O/Ni^{2+} (light green). C) IR spectra of water confined in Ni_2Br_2BTDD from 11 H_2O/Ni^{2+} (dark blue) to 1 H_2O/Ni^{2+} (light blue). All OH stretches are red-shifted by 215 cm^{-1} (Ni_2F_2BTDD and Ni_2Cl_2BTDD) or by 219 cm^{-1} (Ni_2Br_2BTDD).

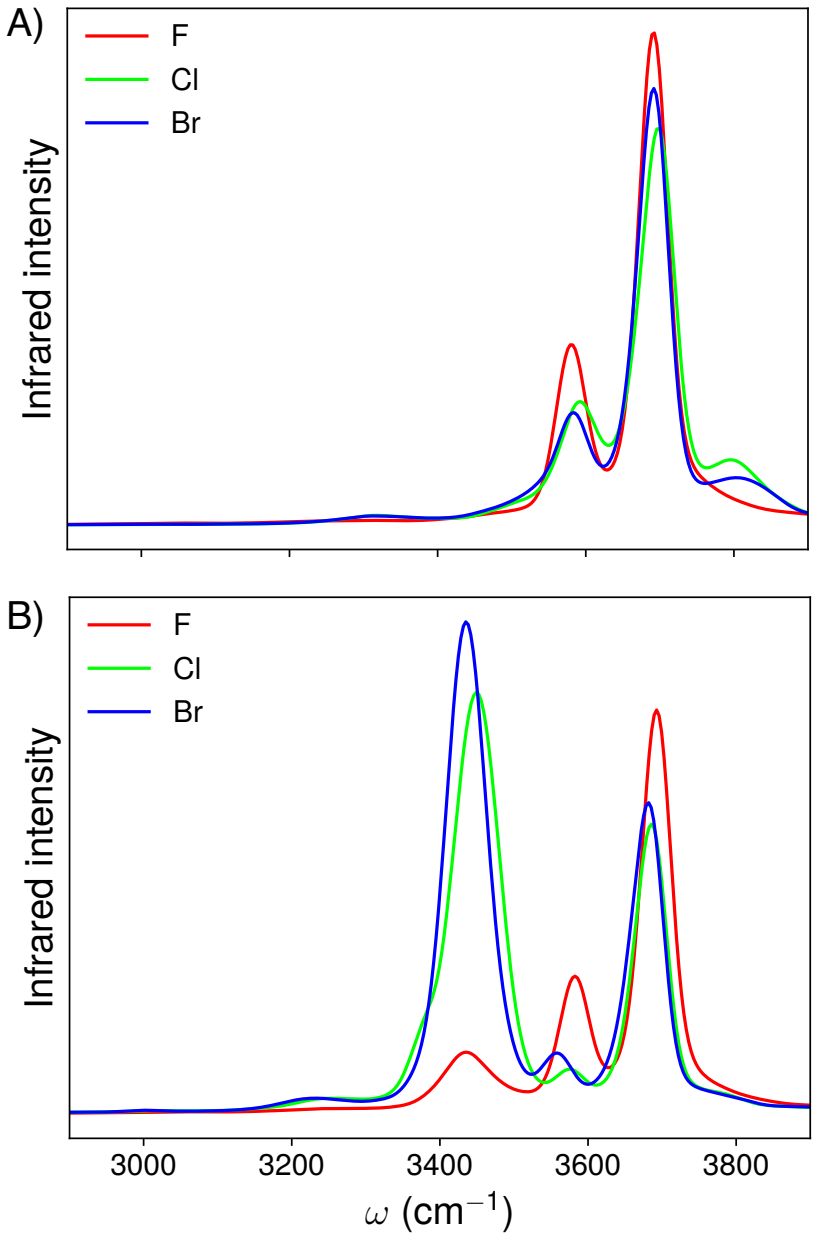

Figure S12: **Infrared spectra of one and two water molecules in Ni_2X_2BTDD.** A) IR spectra of one water molecule in Ni_2F_2BTDD (red), Ni_2Cl_2BTDD (green), and Ni_2Br_2BTDD (blue) MOFs. B) IR spectra of two water molecules in Ni_2F_2BTDD (red), Ni_2Cl_2BTDD (green), and Ni_2Br_2BTDD (blue) MOFs. All OH stretches are red-shifted by 215 cm^{-1} (Ni_2F_2BTDD and Ni_2Cl_2BTDD) or by 219 cm^{-1} (Ni_2Br_2BTDD).

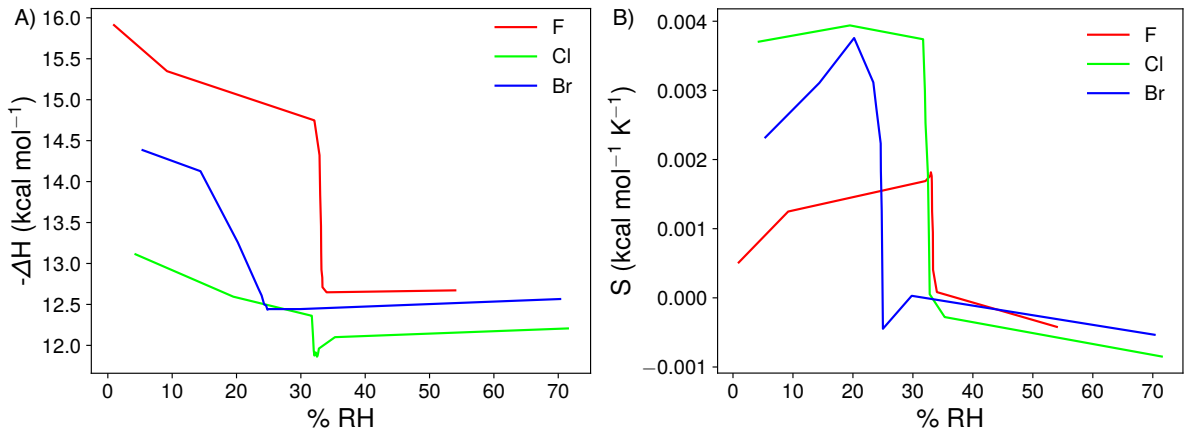

Figure S13: **Enthalpy of adsorption and excess entropy for water in Ni_2X_2BTDD.** A) Simulated enthalpy of adsorption for Ni_2F_2BTDD (red), Ni_2Cl_2BTDD (green), and Ni_2Br_2BTDD (blue) as a function of RH. B) Simulated excess entropy compared to bulk water for Ni_2F_2BTDD (red), Ni_2Cl_2BTDD (green), and Ni_2Br_2BTDD (blue) as a function of RH.

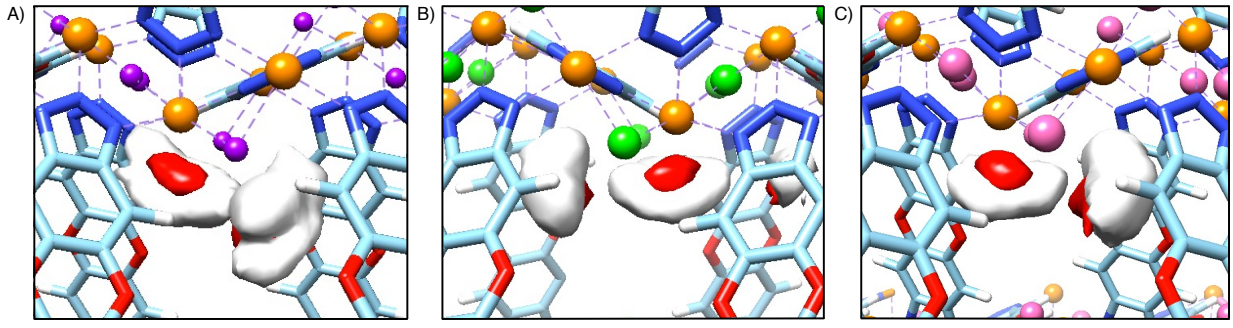

Figure S14: **Spatial distributions of two water molecules in Ni_2X_2BTDD.** Two water molecules adsorbed in A) Ni_2F_2BTDD, B) Ni_2Cl_2BTDD, and C) Ni_2Br_2BTDD. Red isosurfaces correspond to water oxygen atoms, and white isosurfaces correspond to water hydrogen atoms. Color scheme of atoms in panels A through C: Ni – orange, F – purple, Cl – green, Br – pink, N – blue, C – cyan, O – red, H – white.

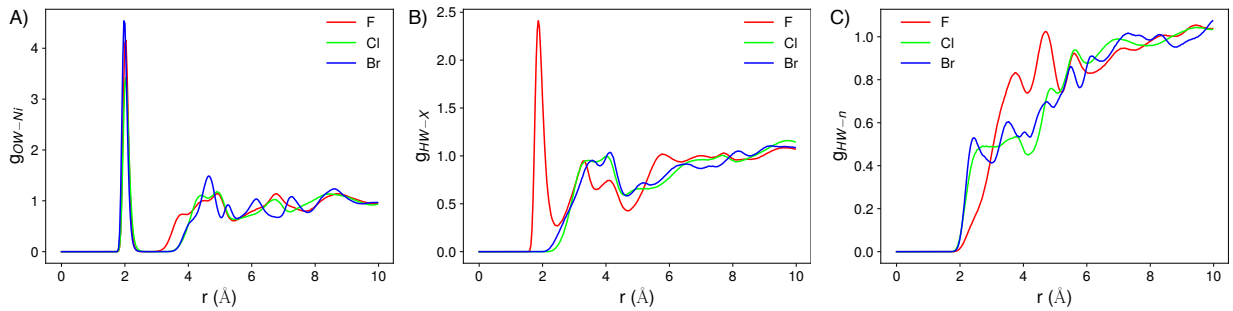

Figure S15: **Radial distribution functions of water in Ni_2X_2BTDD.** A) OW–Ni RDF for Ni_2F_2BTDD (red), Ni_2Cl_2BTDD (green), and Ni_2Br_2BTDD (blue). B) HW–X RDF for Ni_2F_2BTDD (red), Ni_2Cl_2BTDD (green), and Ni_2Br_2BTDD (blue). C) HW–n RDF for Ni_2F_2BTDD (red), Ni_2Cl_2BTDD (green), and Ni_2Br_2BTDD (blue). The RDFs are shown for the maximum loading of each system: 12 H_2O/Ni^{2+} for Ni_2F_2BTDD, 13 H_2O/Ni^{2+} for Ni_2Cl_2BTDD, and 11 H_2O/Ni^{2+} for Ni_2Br_2BTDD.

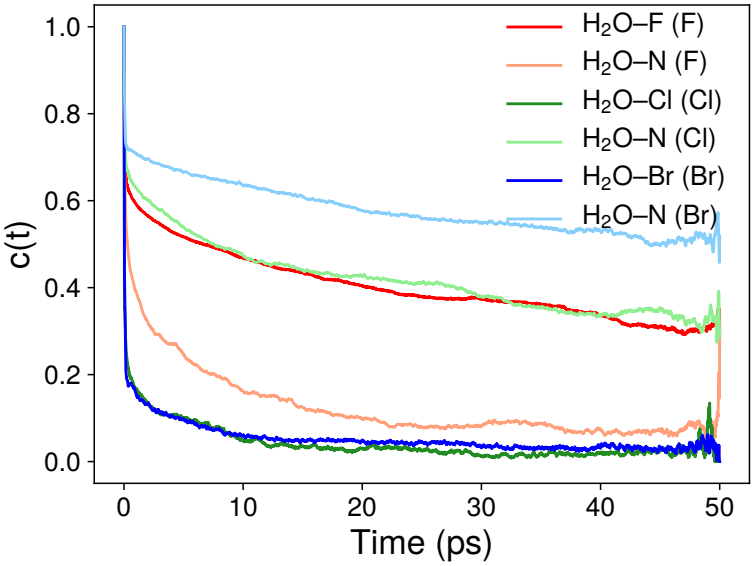

Figure S16: **Hydrogen-bond correlation function for water in Ni_2X_2BTDD.** H-bond correlation function for water donating a H-bond to the F atom in Ni_2F_2BTDD (red), the N atom in Ni_2F_2BTDD (light red), the Cl atom in Ni_2Cl_2BTDD (green), the N atom in Ni_2Cl_2BTDD (light green), the Br atom in Ni_2Br_2BTDD (blue), and the N atom in Ni_2Br_2BTDD (light blue). The H-bond correlation function is shown for the maximum loading of each system: 12 H_2O/Ni^{2+} for Ni_2F_2BTDD, 13 H_2O/Ni^{2+} for Ni_2Cl_2BTDD, and 11 H_2O/Ni^{2+} for Ni_2Br_2BTDD.

References

(1) Babin, V.; Leforestier, C.; Paesani, F. Development of a "First Principles" Water Potential with Flexible Monomers: Dimer Potential Energy Surface, VRT Spectrum, and Second Virial Coefficient. *J. Chem. Theory Comput.* **2013**, *9*, 5395–5403.

(2) Babin, V.; Medders, G. R.; Paesani, F. Development of a "First Principles" Water Potential with Flexible monomers. II: Trimer Potential Energy Surface, Third Virial Coefficient, and Small Clusters. *J. Chem. Theory Comput.* **2014**, *10*, 1599–1607.

(3) Medders, G. R.; Babin, V.; Paesani, F. Development of a "First-Principles" Water Potential with Flexible Monomers. III. Liquid Phase Properties. *J. Chem. Theory Comput.* **2014**, *10*, 2906–2910.

(4) Partridge, H.; Schwenke, D. W. The Determination of an Accurate Isotope Dependent Potential Energy Surface for Water from Extensive Ab Initio Calculations and Experimental Data. *J. Chem. Phys.* **1997**, *106*, 4618–4639.

(5) Braams, B. J.; Bowman, J. M. Permutationally Invariant Potential Energy Surfaces in High Dimensionality. *Int. Rev. Phys. Chem.* **2009**, *28*, 577–606.

(6) Paesani, F. Getting the Right Answers for the Right Reasons: Toward Predictive Molecular Simulations of Water with Many-Body Potential Energy Functions. *Acc. Chem. Res.* **2016**, *49*, 1844–1851.

(7) Reddy, S. K.; Straight, S. C.; Bajaj, P.; Huy Pham, C.; Riera, M.; Moberg, D. R.; Morales, M. A.; Knight, C.; Götz, A. W.; Paesani, F. On the Accuracy of the MB-pol Many-Body Potential for Water: Interaction Energies Vibrational Frequencies and Classical Thermodynamic and Dynamical Properties From Clusters to Liquid Water and Ice. *J. Chem. Phys.* **2016**, *145*, 194504.

(8) Bore, S. L.; Paesani, F. Realistic Phase Diagram of Water from "First Principles" Data-driven Quantum Simulations. *Nat. Commun.* **2023**, *14*, 3349.

(9) Petrenko, V. F.; Whitworth, R. W. *Physics of Ice*; Oxford University Press, Oxford, 1999.

(10) Zhu, X.; Riera, M.; Bull-Vulpe, E. F.; Paesani, F. MB-pol (2023): Sub-chemical Accuracy for Water Simulations from the Gas to the Liquid Phase. *J. Chem. Theory Comput.* **2023**,

(11) Richardson, J. O.; Pérez, C.; Lobsiger, S.; Reid, A. A.; Temelso, B.; Shields, G. C.; Kisiel, Z.; Wales, D. J.; Pate, B. H.; Althorpe, S. C. Concerted Hydrogen-Bond Breaking by Quantum Tunneling in the Water Hexamer Prism. *Science* **2016**, *351*, 1310–1313.

(12) Cole, W. T.; Farrell, J. D.; Wales, D. J.; Saykally, R. J. Structure and Torsional Dynamics of the Water Octamer from THz Laser Spectroscopy Near 215 μm. *Science* **2016**, *352*, 1194–1197.

(13) Mallory, J. D.; Mandelshtam, V. A. Diffusion Monte Carlo Studies of MB-pol $(H_2O)_{2-6}$ and $(D_2O)_{2-6}$ clusters: Structures and Binding Energies. *J. Chem. Phys.* **2016**, *145*, 064308.

(14) Videla, P. E.; Rossky, P. J.; Laria, D. Communication: Isotopic Effects on Tunneling Motions in the Water Trimer. *J. Chem. Phys.* **2016**, *144*, 061101.

(15) Brown, S. E.; Götz, A. W.; Cheng, X.; Steele, R. P.; Mandelshtam, V. A.; Paesani, F. Monitoring Water Clusters "Melt" Through Vibrational Spectroscopy. *J. Am. Chem. Soc.* **2017**, *139*, 7082–7088.

(16) Vaillant, C. L.; Cvitaš, M. T. Rotation-Tunneling Spectrum of the Water Dimer from Instanton Theory. *Phys. Chem. Chem. Phys.* **2018**, *20*, 26809–26813.

(17) Vaillant, C.; Wales, D.; Althorpe, S. Tunneling Splittings from Path-Integral Molecular Dynamics Using a Langevin Thermostat. *J. Chem. Phys.* **2018**, *148*, 234102.

(18) Schmidt, M.; Roy, P.-N. Path Integral Molecular Dynamic Simulation of Flexible Molecular Systems in Their Ground State: Application to the Water Dimer. *J. Chem. Phys.* **2018**, *148*, 124116.

(19) Bishop, K. P.; Roy, P.-N. Quantum Mechanical Free Energy Profiles with Post-Quantization Restraints: Binding Free Energy of the Water Dimer Over a Broad Range of Temperatures. *J. Chem. Phys.* **2018**, *148*, 102303.

(20) Videla, P. E.; Rossky, P. J.; Laria, D. Isotopic Equilibria in Aqueous Clusters at Low Temperatures: Insights from the MB-pol Many-Body Potential. *J. Chem. Phys.* **2018**, *148*, 084303.

(21) Samala, N. R.; Agmon, N. Temperature Dependence of Intramolecular Vibrational Bands in Small Water Clusters. *J. Phys. Chem. B* **2019**, *123*, 9428–9442.

(22) Cvitaš, M. T.; Richardson, J. O. Quantum Tunnelling Pathways of the Water Pentamer. *Phys. Chem. Chem. Phys.* **2020**, *22*, 1035–1044.

(23) Braly, L. B.; Liu, K.; Brown, M. G.; Keutsch, F. N.; Fellers, R. S.; Saykally, R. J. Terahertz Laser Spectroscopy of the Water Dimer Intermolecular Vibrations. II. $(H_2O)_2$. *J. Chem. Phys.* **2000**, *112*, 10314–10326.

(24) Keutsh, F. N.; Goldman, N.; Harker, H. A.; Leforestier, C.; Saykally, R. J. Complete Characterization of the Water Dimer Vibrational Ground State and Testing the VRT(ASP-W)III, SAPT-5st, and VRT(MCY-5f) Surfaces. *Mol. Phys.* **2003**, *101*, 3477–3492.

(25) Keutsch, F. N.; Braly, L. B.; Brown, M. G.; Harker, H. A.; Petersen, P. B.; Lefor-

estier, C.; Saykally, R. J. Water Dimer Hydrogen Bond Stretch, Donor Torsion Overtone, and "In-Plane Bend" Vibrations. *J. Chem. Phys.* **2003**, *119*, 8927–8937.

(26) Zwart, E.; ter Meulen, J.; Meerts, W. L.; Coudert, L. The submillimeter rotation tunneling spectrum of the water dimer. *J. Mol. Spectrosc.* **1991**, *147*, 27 – 39.

(27) Fraser, G. T. $(H_2O)_2$: Spectroscopy, Structure and Dynamics. *Int. Rev. Phys. Chem.* **1991**, *10*, 189–206.

(28) Pérez, C.; Muckle, M. T.; Zaleski, D. P.; Seifert, N. A.; Temelso, B.; Shields, G. C.; Kisiel, Z.; Pate, B. H. Structures of Cage, Prism, and Book Isomers of Water Hexamer from Broadband Rotational Spectroscopy. *Science* **2012**, *336*, 897–901.

(29) Babin, V.; Paesani, F. The Curious Case of the Water Hexamer: Cage vs. Prism. *Chem. Phys. Lett.* **2013**, *580*, 1–8.

(30) Gartner III, T. E.; Hunter, K. M.; Lambros, E.; Caruso, A.; Riera, M.; Medders, G. R.; Panagiotopoulos, A. Z.; Debenedetti, P. G.; Paesani, F. Anomalies and Local Structure of Liquid Water from Boiling to the Supercooled Regime as Predicted by the Many-Body MB-pol Model. *J. Phys. Chem. Lett.* **2022**, *13*, 3652–3658.

(31) Medders, G. R.; Paesani, F. Infrared and Raman Spectroscopy of Liquid Water through "First-Principles" Many-Body Molecular Dynamics. *J. Chem. Theory Comput.* **2015**, *11*, 1145–1154.

(32) Straight, S. C.; Paesani, F. Exploring Electrostatic Effects on the Hydrogen Bond Network of Liquid Water through Many-Body Molecular Dynamics. *J. Phys. Chem. B* **2016**, *120*, 8539–8546.

(33) Reddy, S. K.; Moberg, D. R.; Straight, S. C.; Paesani, F. Temperature-Dependent Vibrational Spectra and Structure of Liquid Water from Classical and Quantum Simulations With the MB-pol Potential Energy Function. *J. Chem. Phys.* **2017**, *147*, 244504.

(34) Hunter, K. M.; Shakib, F. A.; Paesani, F. Disentangling Coupling Effects in the Infrared Spectra of Liquid Water. *J. Phys. Chem. B* **2018**, *122*, 10754–10761.

(35) Sun, Z.; Zheng, L.; Chen, M.; Klein, M. L.; Paesani, F.; Wu, X. Electron-Hole Theory of the Effect of Quantum Nuclei on the X-ray Absorption Spectra of Liquid Water. *Phys. Rev. Lett.* **2018**, *121*, 137401.

(36) Gaiduk, A. P.; Pham, T. A.; Govoni, M.; Paesani, F.; Galli, G. Electron Affinity of Liquid Water. *Nat. Commun.* **2018**, *9*, 1–6.

(37) Cruzeiro, V.; Wildman, A.; Li, X.; Paesani, F. Relationship Between Hydrogen-Bonding Motifs and the $1b_1$ Splitting in the X-ray Emission Spectrum of Liquid Water. *J. Phys. Chem. Lett.* **2021**, *12*, 3996–4002.

(38) Medders, G. R.; Paesani, F. Dissecting the Molecular Structure of the Air/Water Interface from Quantum Simulations of the Sum-Frequency Generation Spectrum. *J. Am. Chem. Soc.* **2016**, *138*, 3912–3919.

(39) Moberg, D. R.; Straight, S. C.; Paesani, F. Temperature Dependence of the Air/Water Interface Revealed by Polarization Sensitive Sum-Frequency Generation Spectroscopy. *J. Phys. Chem. B* **2018**, *122*, 4356–4365.

(40) Sun, S.; Tang, F.; Imoto, S.; Moberg, D. R.; Ohto, T.; Paesani, F.; Bonn, M.; Backus, E. H.; Nagata, Y. Orientational Distribution of Free OH Groups of Interfacial Water is Exponential. *Phys. Rev. Lett.* **2018**, *121*, 246101.

(41) Sengupta, S.; Moberg, D. R.; Paesani, F.; Tyrode, E. Neat Water–Vapor Interface: Proton Continuum and the Nonresonant Background. *J. Phys. Chem. Lett.* **2018**, *9*, 6744–6749.

(42) Muniz, M. C.; Gartner III, T. E.; Riera, M.; Knight, C.; Yue, S.; Paesani, F.; Pana-

giotopoulos, A. Z. Vapor-Liquid Equilibrium of Water with the MB-pol Many-Body Potential. *J. Chem. Phys.* **2021**, *154*, 211103.

(43) Skinner, L.; Benmore, C.; Neuefeind, J.; Parise, J. The Structure of Water Around the Compressibility Minimum. *J. Chem. Phys.* **2014**, *141*, 214507.

(44) Wagner, W.; Pruß, A. The IAPWS Formulation 1995 for the Thermodynamic Properties of Ordinary Water Substance for General and Scientific Use. *J. Phys. Chem. Ref. Data* **2002**, *31*, 387–535.

(45) Holten, V.; Sengers, J. V.; Anisimov, M. A. Equation of State for Supercooled Water at Pressures up to 400 MPa. *J. Phys. Chem. Ref. Data* **2014**, *43*, 043101.

(46) Kell, G. S. Isothermal Compressibility of Liquid Water at 1 atm. *J. Chem. Eng. Data* **1970**, *15*, 119–122.

(47) Speedy, R.; Angell, C. Isothermal Compressibility of Supercooled Water and Evidence for a Thermodynamic Singularity at -45 ^{o}C. *J. Chem. Phys.* **1976**, *65*, 851–858.

(48) Kim, K. H.; Späh, A.; Pathak, H.; Perakis, F.; Mariedahl, D.; Amann-Winkel, K.; Sellberg, J. A.; Lee, J. H.; Kim, S.; Park, J., et al. Maxima in the Thermodynamic Response and Correlation Functions of Deeply Supercooled Water. *Science* **2017**, *358*, 1589–1593.

(49) Pham, C. H.; Reddy, S. K.; Chen, K.; Knight, C.; Paesani, F. Many-Body Interactions in Ice. *J. Chem. Theory Comput.* **2017**, *13*, 1778–1784.

(50) Moberg, D. R.; Straight, S. C.; Knight, C.; Paesani, F. Molecular Origin of the Vibrational Structure of Ice I_h. *J. Phys. Chem. Lett.* **2017**, *8*, 2579–2583.

(51) Moberg, D. R.; Sharp, P. J.; Paesani, F. Molecular-Level Interpretation of Vibrational Spectra of Ordered Ice Phases. *J. Phys. Chem. B* **2018**, *122*, 10572–10581.

(52) Wang, J.; Wolf, R. M.; Caldwell, J. W.; Kollman, P. A.; Case, D. A. Development and Testing of a General Amber Force Field. *J. Comput. Chem.* **2004**, *25*, 1157–1174.

(53) Frisch, M. J.; Trucks, G. W.; Schlegel, H. B.; Scuseria, G. E.; Robb, M. A.; Cheeseman, J. R.; Scalmani, G.; Barone, V.; Petersson, G. A.; Nakatsuji, H.; Li, X.; Caricato, M.; Marenich, A. V.; Bloino, J.; Janesko, B. G.; Gomperts, R.; Mennucci, B.; Hratchian, H. P.; Ortiz, J. V.; Izmaylov, A. F.; Sonnenberg, J. L.; Williams-Young, D.; Ding, F.; Lipparini, F.; Egidi, F.; Goings, J.; Peng, B.; Petrone, A.; Henderson, T.; Ranasinghe, D.; Zakrzewski, V. G.; Gao, J.; Rega, N.; Zheng, G.; Liang, W.; Hada, M.; Ehara, M.; Toyota, K.; Fukuda, R.; Hasegawa, J.; Ishida, M.; Nakajima, T.; Honda, Y.; Kitao, O.; Nakai, H.; Vreven, T.; Throssell, K.; Montgomery, J. A., Jr.; Peralta, J. E.; Ogliaro, F.; Bearpark, M. J.; Heyd, J. J.; Brothers, E. N.; Kudin, K. N.; Staroverov, V. N.; Keith, T. A.; Kobayashi, R.; Normand, J.; Raghavachari, K.; Rendell, A. P.; Burant, J. C.; Iyengar, S. S.; Tomasi, J.; Cossi, M.; Millam, J. M.; Klene, M.; Adamo, C.; Cammi, R.; Ochterski, J. W.; Martin, R. L.; Morokuma, K.; Farkas, O.; Foresman, J. B.; Fox, D. J. Gaussian˜16 Revision A.03. 2016; Gaussian Inc. Wallingford CT.

(54) Chai, J.-D.; Head-Gordon, M. Long-Range Corrected Hybrid Density Functionals With Damped Atom–Atom Dispersion Corrections. *Phys. Chem. Chem. Phys.* **2008**, *10*, 6615–6620.

(55) Weigend, F.; Ahlrichs, R. Balanced Basis Sets of Split Valence Triple Zeta Valence and Quadruple Zeta Valence Quality for H to Rn: Design and Assessment of Accuracy. *Phys. Chem. Chem. Phys.* **2005**, *7*, 3297–3305.

(56) Lin, S.-T.; Blanco, M.; Goddard III, W. A. The Two-Phase Model for Calculating Thermodynamic Properties of Liquids From Molecular Dynamics: Validation for the Phase Diagram of Lennard-Jones Fluids. *J. Chem. Phys.* **2003**, *119*, 11792–11805.

(57) Lin, S.-T.; Maiti, P. K.; Goddard III, W. A. Two-Phase Thermodynamic Model for Efficient and Accurate Absolute Entropy of Water From Molecular Dynamics Simulations. *J. Phys. Chem. B* **2010**, *114*, 8191–8198.

(58) Pascal, T. A.; Lin, S.-T.; Goddard III, W. A. Thermodynamics of Liquids: Standard Molar Entropies and Heat Capacities of Common Solvents From 2PT Molecular Dynamics. *Phys. Chem. Chem. Phys.* **2011**, *13*, 169–181.

(59) Luzar, A.; Chandler, D. Hydrogen-Bond Kinetics in Liquid Water. *Nature* **1996**, *379*, 55–57.